Metals & corrosion

Effect of SiC nanoparticles on the precipitation behavior and mechanical properties of 7075Al alloy

Bowen Pu[1], Xiaobin Lin[1], Bowen Li[1], Xiaofeng Chen[1], Chunnian He[1,2,*] (iD), and Naiqin Zhao[1,2,*] (iD)

[1] School of Materials Science and Engineering and Tianjin Key Laboratory of Composite and Functional Materials, Tianjin University, Tianjin 300350, People's Republic of China
[2] Collaborative Innovation Centre of Chemical Science and Engineering, Tianjin 300072, People's Republic of China

ABSTRACT

In terms of aluminum alloy matrix composites, the effect of reinforcement on precipitation is worth investigating. In this work, the silicon carbide nanoparticles-reinforced 7075Al (SiC_{np}/7075Al) composite was fabricated through a series of powder metallurgy procedures, shift-speed ball milling, hot pressing, and hot extrusion, and the precipitation behavior of SiC_{np}/7075Al composite was compared with that of 7075Al alloy after T6 treatment. The results show that only a small addition (1 vol%) of SiC_{np} modifies the morphology and dispersion of precipitates. The uniformly dispersed small precipitates (η' phase) and increased dislocation density have a positive influence on the mechanical properties of composites. Based on the fracture surface and element composition, a fracture mode dominated by precipitated phase-induced crack initiation was proposed. This study suggests a promising approach to design the alloy matrix composites through controlling the behavior of precipitated phases with nano-reinforcement.

Introduction

As a kind of heat-treatment strengthening aluminum alloys, 7xxx aluminum (7xxxAl) alloys are drawing significant attention because of their high specific strength and stiffness. They are considered having a wide application in the fields of aerospace, automotive, weapons, and transportation [1–3]. To increase the mechanical properties of 7xxxAl alloys, many investigations have been focused on the design of chemical composition and heat treatment in the past decades [4, 5]. Recent decade, thermo-mechanical processing consisting of plastic deformation and heat treatment has received much attention recently not only to improve the strength of age-hardening Al alloys but also to obtain feasible industrial applications [2–4, 6]. As a typical Al–Zn–Mg–Cu alloy, 7075Al alloy has been extensively studied under thermo-mechanical treatments and the precipitation sequence is always followed by supersaturated solid solution $\rightarrow$ GP zone $\rightarrow \eta' \rightarrow \eta$ ($MgZn_2$), where the

Address correspondence to E-mail: cnhe08@tju.edu.cn; nqzhao@tju.edu.cn

Springer

spherical GP zones are fully coherent with matrix and generally form in the early stage of artificial aging, the plate-shaped η′ phase is a semi-coherent intermediate phase with hexagonal structure and form taking GP zones as nucleation sites, and η-phase is also a hexagonal plate-shaped phase but incoherent with the matrix [4, 6–9]. It has been found that the η′ phase is the mainly responsible precipitate for strengthening of 7075Al alloys at the peak-aging condition [8].

Besides, the compositing approach has an increasing appeal to materials researchers to improve the elastic modulus and other comprehensive properties of Al alloy matrix, especially with the particulate reinforcements [10–12]. In fact, size and volume fraction are two main parameters for particulate reinforcements [10, 13]. Guo et al. [14] found small particles were beneficial to load-transfer capability through the interface in composites and achieving an enhanced strength. In contrast to the easy stress concentration in micron-particles/metal matrix composites, nano-sized reinforcements play a critical role in dispersing stress and decreasing stress localization [15], while with the increase in addition, particles usually lose their capability to homogeneous distribution and are prone to the formation of clusters, especially the nano-sized particles. Therefore, nanoparticles-reinforced Al alloy matrix composites were often fabricated with a low volume fraction (below 2%) of reinforcement to gain an effective dispersion [10–12, 16].

Inspired by the work of Xu et al. [17, 18], powder metallurgy, especially assisted by shift-speed ball milling, provides a better preparation strategy to avoid the problems of interfacial reaction and particles settling by traditional casting or semi-solid forming [11, 12, 19]. Nevertheless, most of the published literature at present lays partial emphasis on the strengthening effect of either reinforcements or matrix precipitates [4, 10–12]. There is little research studied on the roles of precipitation behaviors related to nano-reinforcements in the mechanical properties of Al alloy matrix composites. Among diverse kinds of ceramic particulates, silicon carbide (SiC) has several outstanding advantages and the characteristics of polymorphism. Its polymorphs of 3C-, 2H-, 4H- and 6H- have cubic structure, hexagonal structure, hexagonal/cubic mixed structure and rhombic structure, respectively. In particular, 6H-SiC with a high melting point, high thermal conductivity, high

chemical stability, as well as irradiation effect, still possesses widespread promising prospects of research [20, 21].

In this study, 7075Al composites reinforced by small addition of SiC_{np} were fabricated by shift-speed ball milling method combined with hot pressing, hot extrusion, and T6 heat treatment. The mechanical properties and microstructural characteristics of materials were studied, and the precipitation behavior SiC_{np}/7075Al composite was analyzed and discussed in detail. The strengthening mechanism and fracture mode caused by optimized precipitation behavior were also investigated. The present work is expected to open sight of interaction effects between nano-fillers and precipitates in Al alloy matrix composites.

Experimental

Raw materials

The morphologies of the raw materials are shown in Fig. 1. Atomized spherical 7075 aluminum alloy powders (Fig. 1a) were provided by Titd Metal Materials Co., Ltd. (Changsha, China). The main chemical composition of the 7075Al alloy powders (density: 2.8 g/cm^3) is Al–5.6 Zn–2.5 Mg–1.6 Cu (wt%), and that of the other microalloying elements (such as Fe, Mn, Cr, and Zr) is less than 2.0 wt%. The α-SiC nanoparticles (SiC_{np}, density: 3.2 g/cm^3) were purchased from DK Nano Science and Technology Co. Ltd. (Beijing, China) and spontaneously tend to form clusters, as shown in Fig. 1b. The statistical average diameters of the 7075Al alloy powders and SiC_{np} are ∼ 10 μm (Fig. 1c) and ∼ 50 nm (Fig. 1d), respectively.

Fabrication process of composites

The shifting speed of ball milling was used to disperse the SiC_{np} into 7075Al powders. The SiC_{np} and 7075Al powders were first ball-milled together with a low-speed ball milling of 250 rpm/min for 4 h under the protection of Ar atmosphere, and then the mixing process was performed with a high-speed ball milling of 500 rpm/min for 0.5 h to make the spherical matrix powders slightly cold-welded and deformed. The ball-to-powder weight ratio was always 20:1, and 1 wt% stearic acid was added as process control

Figure 1 SEM images of **a** raw 7075Al alloy powders, **b** raw SiC_{np}, and **c**, **d** the statistics charts of their sizes in diameter.
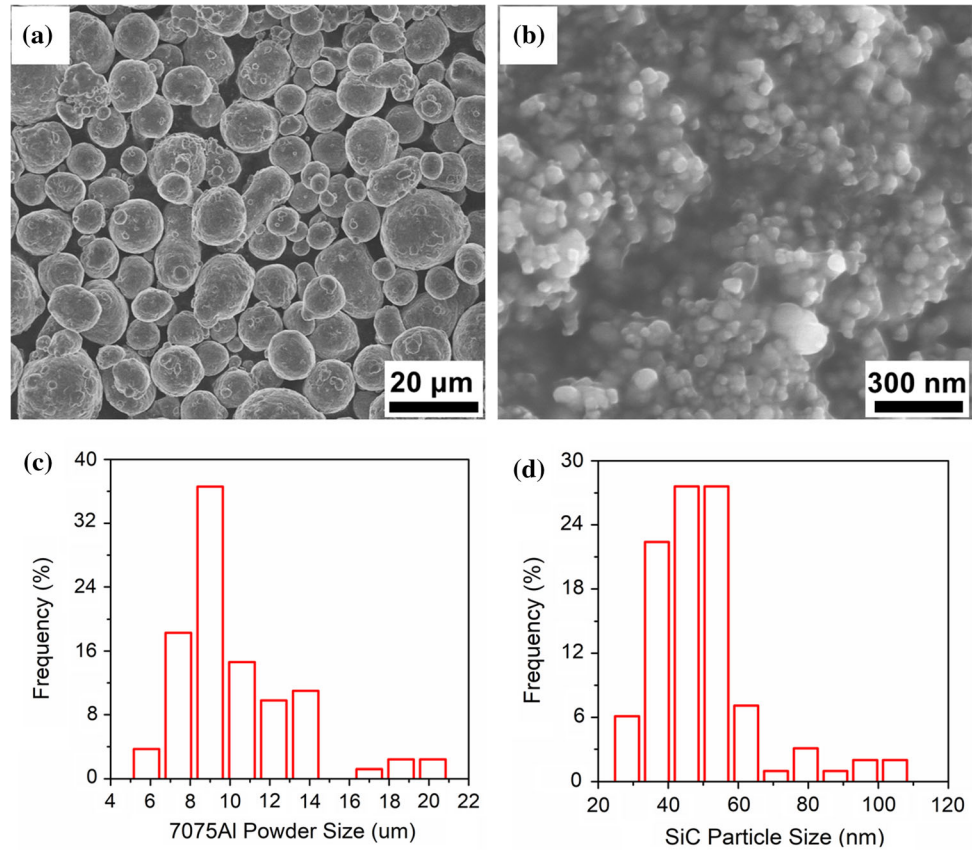
agent (PCA). The volume fraction of the SiC_{np} in composite powders was designed as 0.5, 1.0, and 1.5%. The as-obtained composite powders were cold-pressed (600 MPa, 3 min) in cylinder steel die (diameter 20 mm) to form compacts. The subsequent thermo-mechanical and heat-treatment processing is illustrated in Fig. 2. The cylindrical compacts were hot-press sintered at 520 °C in vacuum condition, holding for 60 min under the pressure of 50 MPa. The sintered bulk composites were extruded with an extrusion ratio of 16:1 after preheating in a muffle furnace at 500 °C for 30 min. The extruded samples were subjected to T6 (480 °C/1 h + water quenching + 120 °C/24 h) heat treatments.

Characterization

The morphology of powders samples and fracture surfaces was investigated using a scanning electron microscope (SEM, Hitachi S-4800). The microstructures of sintered and extruded samples were observed through an optical microscope (OM, Leica DM 2700 M). The transmission electron microscope (TEM, JEM-2100F) including scanning TEM (STEM)
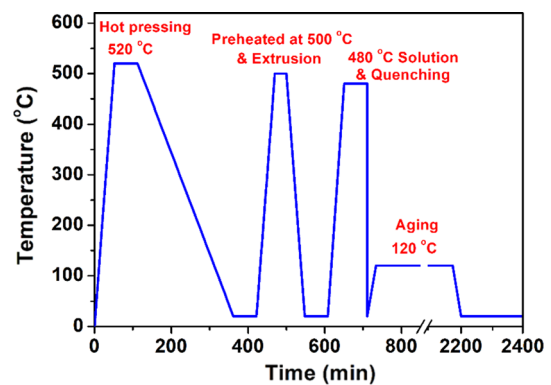
Figure 2 Schematic presentations of thermo-mechanical and heat-treatment processing.

and energy-dispersive X-ray spectroscopy (EDS) were used to observe the distributions and morphology characteristics of SiC_{np} and precipitates. The TEM samples ($\sim$ 3 mm in diameter) were prepared through mechanically polishing and ion milling on a precision ion polishing system (Gatan-PIPS695). X-ray diffractometer (XRD, Bruker D8 Advanced) with a Cu Kα radiation source was utilized to determine the phase composition and evaluate the

dislocation densities of the samples. The tensile testing experiments were performed by a standard mechanical tester (Lloyd (AMETEK) EZ 20) with a crosshead speed of 0.5 mm min^{-1} at room temperature. For tensile testing, an extruded rod-shaped bulk sample was machined on a lathe into a dumbbell-like specimen with a gauge of 15 mm in length and 3 mm in diameter. The hardness of the samples was measured by an MH-6 hardness detector (load = 500 N, dwell time = 5 s).

Results

The morphology of ball-milled powders, as-sintered, and extruded composites

Figure 3a–d shows the morphology comparison of 7075Al and SiC$_{np}$/7075Al composite powders with different SiC$_{np}$ contents via shift-speed ball milling. All the powders were flattened into the thick sheet-like shape. The high-magnified SEM images of their surfaces in Fig. 3e–h show the dispersion states of SiC$_{np}$, and there is no obvious agglomeration of SiC$_{np}$. It could be seen that most of the SiC$_{np}$ were uniformly dispersed on the surface of Al powders, especially for the content of 0.5 vol% (Fig. 3e). Although some small clusters were found on 1.0 and 1.5 vol% SiC$_{np}$/7075Al composite powders, as indicated by the arrows in Fig. 3g, h, the corresponding elemental maps of Al, Si, and C (Fig. 3i–l) revealed the evenly dispersed SiC$_{np}$ on Al matrix.

Figure 4 shows the OM microstructures of the 7075Al alloy matrix and 1.0 vol% SiC$_{np}$/7075Al composite after hot-press sintering. Both the unreinforced alloy (Fig. 4a, c) and SiC$_{np}$/7075Al composite (Fig. 4b, d) were densified, and no defects and voids were observed. Etched by Keller's reagent for 1 min, the grain boundaries of the composite preferentially tended to be exposed (Fig. 4b). The coarse pre-precipitated phases were mainly distributed at grain boundaries and also randomly located in the grain of the alloy matrix and composite (Fig. 4c, d). However, the number of pre-precipitated phases in the composite was more than that in the alloy matrix and the grain migration of composite was impeded by SiC$_{np}$ causing a grain refinement effect. Figure 4e, f shows the three-dimensional OM images of the extruded 7075Al alloy and 1.0 vol% SiC$_{np}$/7075Al composite. The cylinder surface toward the extrusion direction

(ED) and the cross section on the radial direction (RD) were each observed and then combined together to reveal the spatial morphology of grains and the shape of extruded samples. Some elongated grains could be observed on both surfaces of them parallel to the ED, while equiaxed grains were found on the cross section. SiC$_{np}$ exhibited an orientation distribution with the plastic flow of alloy matrix during the hot-extrusion process.

### Distribution and identification of reinforcement particles

Figure 5a shows the XRD pattern of the original SiC$_{np}$. The strong peaks were identified to be the phase of hexagonal 6H-SiC (PDF Card No. 75-1541) [20]. The regular-shaped SiC$_{np}$ have a narrow size of distribution and superior crystallinity (Fig. 5b, c), and the measured interspacing in Fig. 5c is ~ 0.251 nm, which is corresponding to the d-spacing of (006) plane of the typical hexagonal SiC. As shown in Fig. 5d, a large number of precipitates were found both in the grain and at the grain boundaries (marked by yellow dotted lines) of T6-treated composites. To identify the distribution of SiC$_{np}$ in the composites, the EDS analysis was performed to the whole region of Fig. 5d, exhibiting the enrichment area of Si element around the grain boundary (Fig. 5e). It has been reported that the interface of the Al/SiC composites prepared by powder metallurgy was chemically stable without the formation of the Al$_4$C$_3$ phase when the processing temperature below 650 °C [22]. Therefore, the enriched Si element in the EDS mapping was supposed to be the SiC$_{np}$. Although the SiC$_{np}$ preferentially exist at the grain boundary, there are no porosities between the SiC$_{np}$ and the 7075Al matrix.

Tensile behaviors and mechanical properties

To demonstrate the proper aging time we used, the evolutions of Vickers microhardness of the 7075Al alloy and 1.0 vol% SiC$_{np}$/7075Al were operated during isothermal aging at 120 °C (Fig. S1). The hardness value of the composite was always higher than that of alloy matrix on the condition of both solid-solution and aging processes. The peak hardness was achieved after aging for 24 h, and the peak
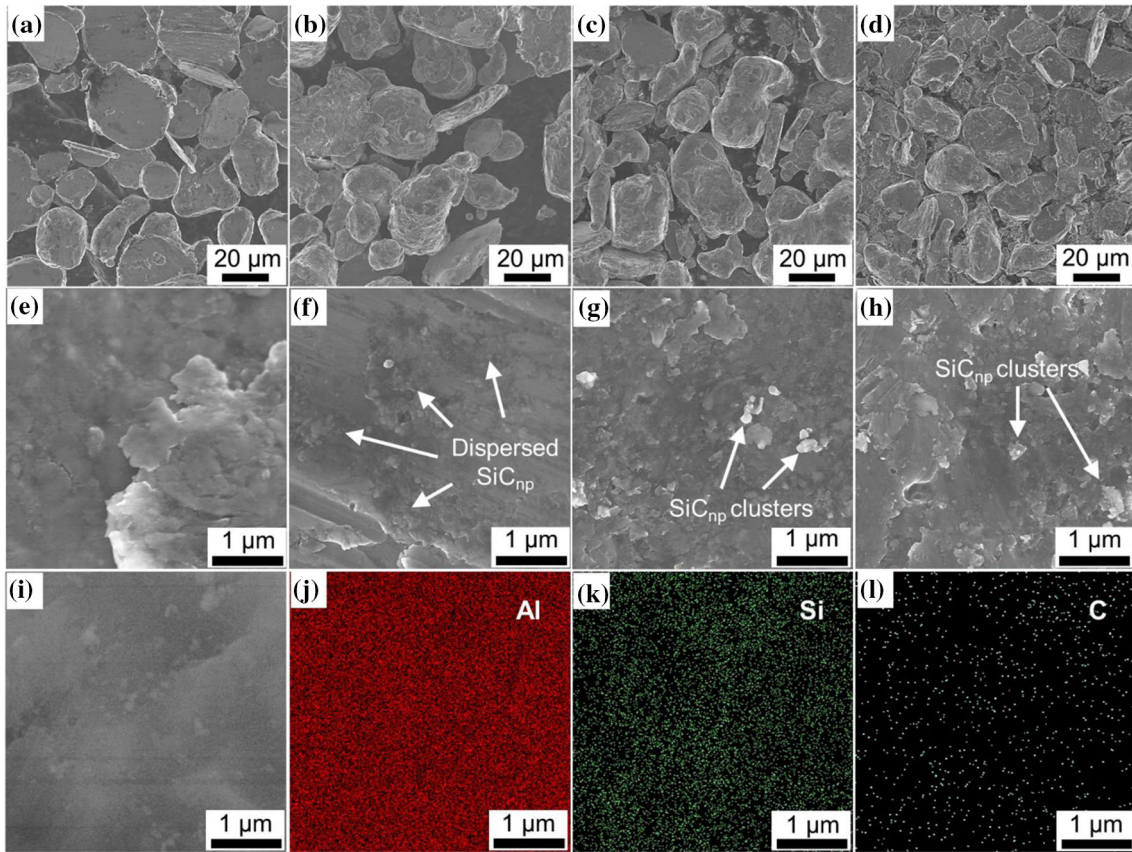
Figure 3 The representative SEM images and corresponding surface morphologies of SiC$_{np}$/7075Al powders with various contents of SiC$_{np}$: **a**, **e** 0, **b**, **f** 0.5 vol%, **c**, **g** 1.0 vol%, and **d**, **h** 1.5 vol% via shift-speed ball milling. The EDS mapping analysis on **i** the surface of 1.0 vol% SiC$_{np}$/7075Al powders: **j**–**l** the corresponding elements of Al, Si, and C distribution.
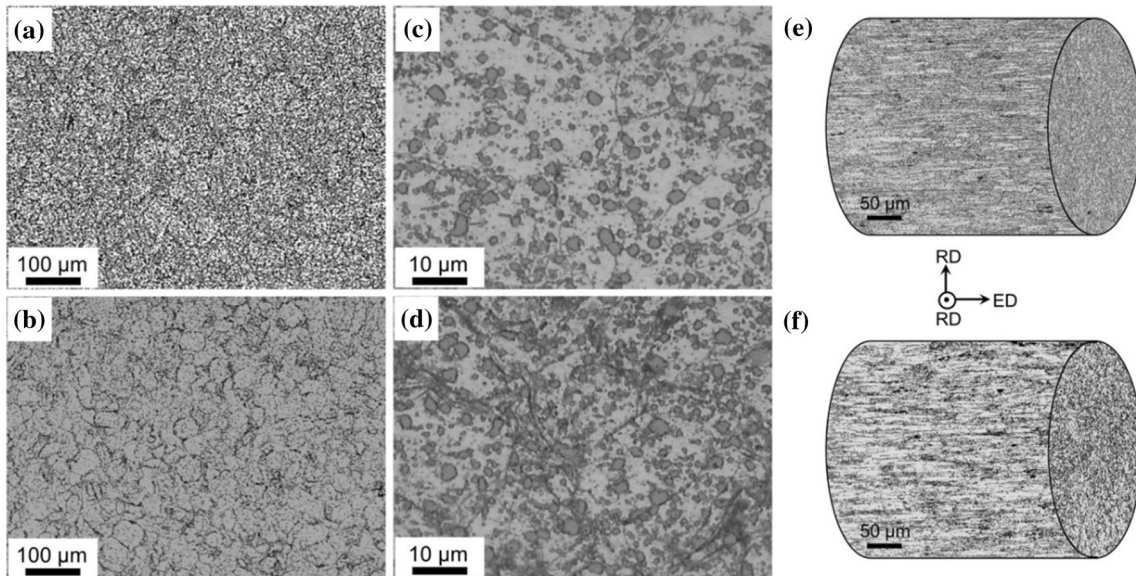
Figure 4 Optical micrographs of hot-press sintered (**a**, **c**) 7075Al alloy and (**b**, **d**) 1.0 vol% SiC$_{np}$/7075Al composite. Three-dimensional images of optical microstructure of **e** 7075Al alloy and **f** 1.0 vol% SiC$_{np}$/7075Al composite, where ED and RD stand for the extrusion and radial directions, respectively.
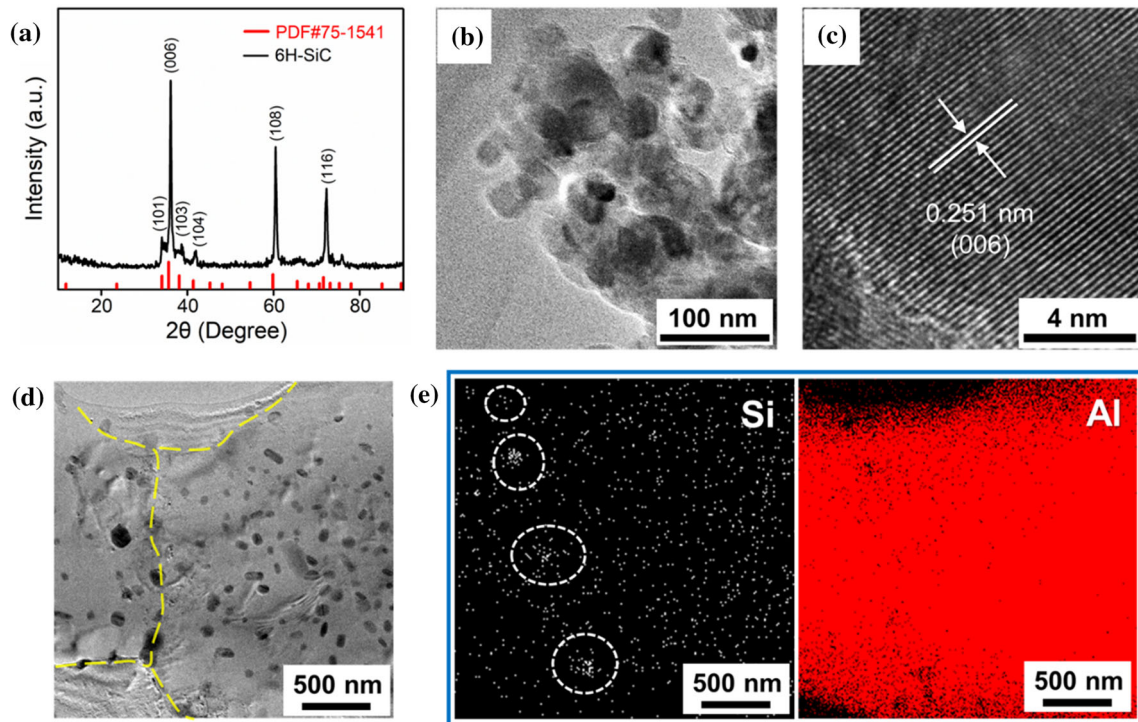
Figure 5 a XRD pattern of the original 6H-SiC; **b, c** TEM images of the microstructure of SiC nanoparticles; **d, e** TEM bright-field image and EDS mapping (elements of Si and Al) for the distributions of SiC nanoparticles in the composite.

hardness of the 7075Al alloy and 1.0 vol% SiC_{np}/7075Al was 175.3 and 182.5 HV, respectively.

The representative tensile stress–strain curves of peak-aged 7075Al alloy and SiC_{np}/7075Al composites with different SiC_{np} contents are displayed in Fig. 6a. The inset diagram shows the shape and size of the tensile specimen. At the first stage, the stress presented linearly elastic loading up to the yielding point with the increase in tensile strain. Subsequently, a strain hardening process appeared until reaching the maximum value of stress. The elongations from peak stress to fracture were little, for the alloy matrix, and its composites were too rigid to produce flow stress and necking deformation. Figure 6b shows the variations of yield strength (YS) and ultimate tensile strength (UTS) with the amount of SiC_{np}, and the average values and errors of the tensile properties are listed in Table S1. With the increase in the addition of SiC_{np} into 7075Al alloy, the YS and UTS of SiC_{np}/7075Al composites increased and reached a maximum value of YS of 559 MPa and UTS of 609 MPa for 1.0 vol% SiC_{np}/7075Al composite, which improved 72 MPa and 53 MPa compared with matrix, respectively. Although the YS and UTS decreased to 505 MPa and 573 MPa with SiC_{np}

content of 1.5 vol%, the encouraging improvements of YS and UTS under such a small addition of SiC_{np} manifested an excellent reinforced effect for the 7075Al alloy matrix.

Microstructures and precipitation characteristics of 7075Al and SiC_{np}/7075Al composites

Figure 7 depicts typical bright-field TEM, STEM (selected area marked by yellow and white boxes), and corresponding EDS mapping distributions of peak-aged 7075Al alloy and 1 vol% SiC_{np}/7075Al composite. From Fig. 7a–c, precipitates can be observed within the grains and at the grain boundaries in 7075Al alloy and the coarse precipitate zone (CPZ) and precipitate-free zone (PFZ) are also visible in the image. The CPZ are usually related to equilibrium η phases preferentially located at grain boundaries [8, 23]. EDS analysis showed Zn and Mg were rich at both coarsened precipitates along the grain boundaries and fine well-dispersed precipitates within the grains. The element of Cu was also found at the precipitates, which may be because the diffusivity of Cu atom was slower than that of Mg and Zn atoms in

Figure 6 **a** Representative engineering stress–strain curves of T6-treated 7075Al alloy and SiC$_{np}$/7075Al bulk composites, where the inset shows the dimension of the specimen used for tensile test. **b** Relationships of YS and UTS with the SiC$_{np}$ content.
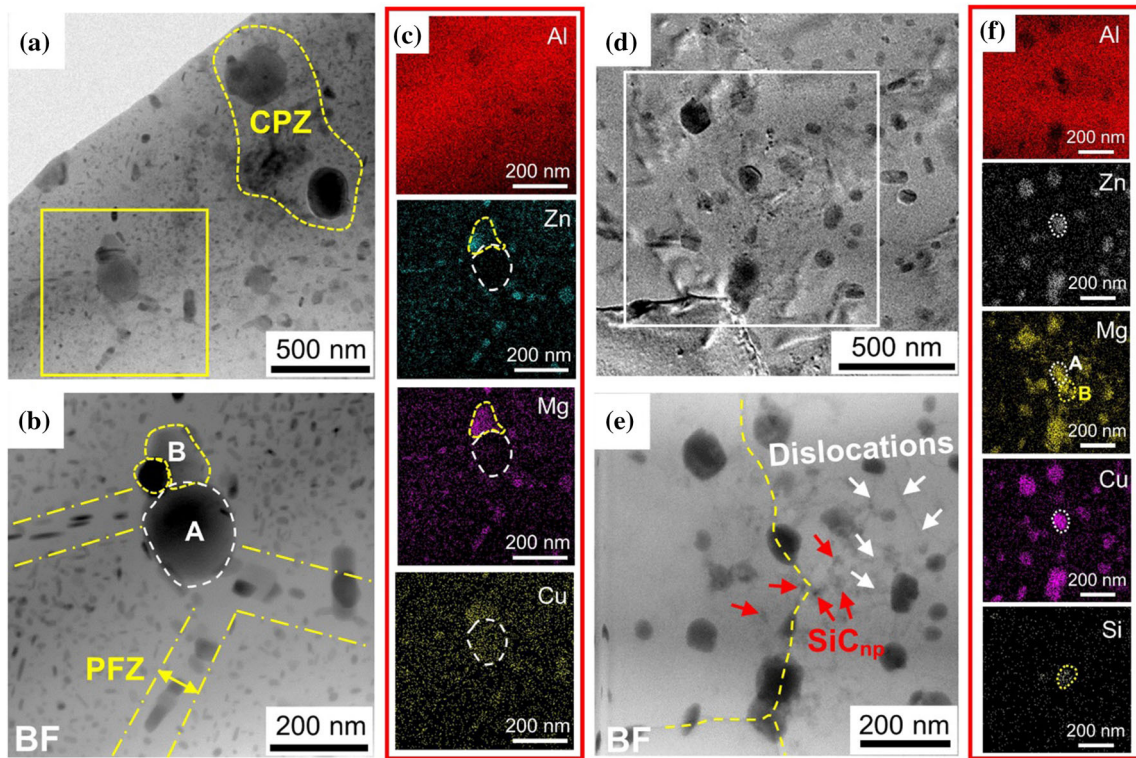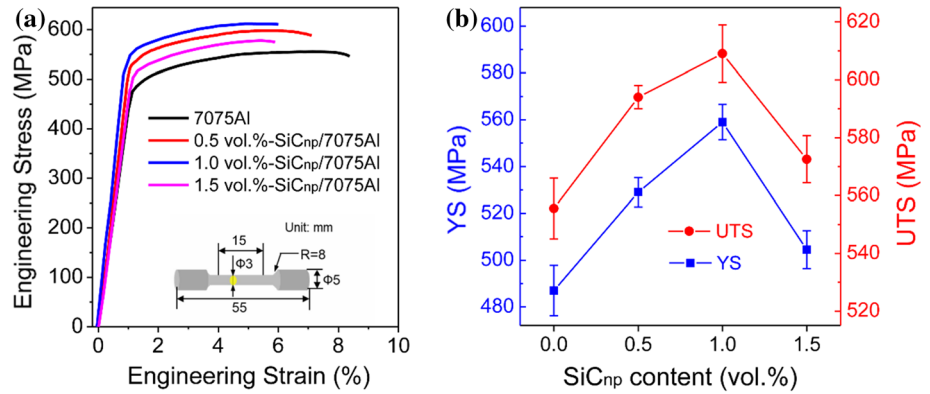
Figure 7 Microstructure of 7075Al alloy and 1 vol% SiC$_{np}$/7075Al composite. TEM images, bright-field scanning TEM (BF-STEM) images, and high-resolution EDS of Al, Zn, Mg, Cu, and Si maps for **a–c** 7075Al and **d–f** SiC$_{np}$/7075Al composite.

Al, resulting in a further clustered [5]. Notably, a coarse precipitate (A in Fig. 7b) was enriched with Cu, but almost no Zn and Mg at it. The polygon-shaped precipitate (B in Fig. 7b) besides the coarse precipitate A had a large amount of Zn and Mg. The same results were also seen in the EDS line-scan across a position of the precipitated particle (Fig. S2a–d). Some irregular precipitates appear at the edge of the segregation area of Cu, the detected composition of which suggests that the atom ratio of Zn/Mg is close to 2/1. Therefore, the main nucleation mechanism of MgZn$_2$ precipitates is thought that Mg and Zn atoms enrich on the edges of Cu-contained pre-precipitates. Figure 7d–f displays precipitates in SiC$_{np}$/7075Al composite with uniform size and no discernible CPZ or PFZ. From EDS mapping results (Fig. 7f), the distribution of the elements Zn, Mg, and Cu is similar to those in 7075Al alloy, corresponding to the precipitates in the STEM micrograph (Fig. 7e), while Mg atoms show an aggregation not only at the precipitates (A in Fig. 7f) but also in the vicinity of SiC$_{np}$ reinforcements (B in Fig. 7f), probably

concerning the tendency to form Mg_2Si or interfacial phase of MgO reported in the previous literature [24–26]. As shown in Fig. 7e, the SiC_{np} (marked by red arrows) were prone to pile up at the grain boundary (marked by yellow dash line) with a lot of induced dislocations (marked by white arrows) adjacent to it.

Figure 8a–c shows the representative TEM and HRTEM images of precipitation characteristic in peak-aged 7075Al alloy. The combination of η' phases (marked by white arrows in Fig. 8a) and GP zones (marked by yellow arrows in Fig. 8a) with a continuous distribution was observed in the grain interior, which are generally the main precipitates of 7075Al alloy in strengthening at T6 heat treatment [8]. At the same time, some coarse precipitates also presented along the grain boundary, implying a discontinuous distribution of the CPZ. From the analysis of crystal structure, η' phase has the typical shape of hexagon (Fig. 8b and Fig. S2e, f) and GP zone in size of $\sim$ 10 nm is coherent with the Al matrix (Fig. 8c). Compared with 7075Al alloy, the precipitation behavior in peak-aged SiC_{np}/7075Al composite shows a distribution of uniform-sized precipitates without obvious PFZ and CPZ (Fig. 8d). The η' phase in SiC_{np}/7075Al composite still had the hexagonal structure but grew into a lath-shaped platelet with increasing diameter (Fig. 8e). GP zones were smaller and $\sim$ 5 nm in size, exhibiting a dense distribution in grain interior (Fig. 8f). One platelet-shaped precipitate in the SiC_{np}/7075Al composite was selected to further confirm by crystallographic analysis, the HRTEM image of which is shown in Fig. 8g. Figure 8g1 is the inverse fast Fourier transform (IFFT) of an enlarged portion of the white dash box in Fig. 8g, and the corresponding fast Fourier transform (FFT) is displayed in Fig. 8g2. Combined with clear diffraction streaks in FFT, the inter-planar spacings of the feature lattice fringes in Fig. 8g1 were measured to be $\sim$ 0.232 and $\sim$ 0.437 nm, in consistence with the d-spacing of $(1\bar{2}12)_{\eta'}$ (equal to d $11\bar{1}$ Al) and $(10\bar{1}0)_{\eta'}$ (equal to 1/3 d $\bar{2}20$ Al), respectively [5, 8, 23]. The crystallographic relationship between η' phase and Al matrix along the projected direction of $[\bar{1}2\bar{1}3]_{\eta'}$ (parallel to $[112]_{Al}$) is $(1\bar{2}12)_{\eta'}//(11\bar{1})_{Al}$ and $(10\bar{1}0)_{\eta'}//(\bar{2}20)_{Al}$, as illustrated by the simulated diffraction pattern in Fig. 8g3. The attached growth state of two categories of precipitates was also

observed by HRTEM (Fig. 8h). The IFFT of the yellow dash box in Fig. 8h was conducted, where the different structural characteristics between these two precipitates were detected and marked by green and white dash lines, respectively (Fig. 8h1). Their corresponding FFT patterns are shown in Fig. 8h2 and h3. Based on the FFT and IFFT images of the marked regions, η' phase and Al_2Cu phase were identified and the angle between $(1\bar{2}12)_{\eta'}$ and $(\bar{1}\bar{1}2)_{Al_2Cu}$ planes was shown to be 12.8°. The atomic misfits of $(1\bar{2}12)_{\eta'}$ and $(\bar{1}\bar{1}2)_{Al_2Cu}$ can be estimated as [15, 27]:

$$\varepsilon = \frac{\left| d_{(1\bar{2}12)_{\eta'}} \cos\theta - d_{(\bar{1}\bar{1}2)_{Al_2Cu}} \right|}{d_{(\bar{1}\bar{1}2)_{Al_2Cu}}} \times 100\% \qquad (1)$$

where θ is the angle between $(1\bar{2}12)_{\eta'}$ and $(\bar{1}\bar{1}2)_{Al_2Cu}$ planes, $d_{(1\bar{2}12)\eta'}$ is 0.235 nm, and $d_{(\bar{1}\bar{1}2)Al_2Cu}$ is 0.212 nm. The calculated misfit between $(\bar{1}\bar{1}2)_{Al_2Cu}$ and $(\bar{1}\bar{1}2)_{Al_2Cu}$ is $\sim$ 8.09% ($<$ 25%), suggesting that the interface between these two phases is semi-coherent [27, 28]. The assumed nucleation process of Mg and Zn atoms was proved that they clustered on the edges of Cu-contained pre-precipitates and precipitated along the special crystal surface.

X-ray diffraction analysis and dislocation density

XRD patterns of the RD surfaces of as-quenched 7075Al, as-quenched 1 vol% SiC_{np}/7075Al, T6-treated 7075Al, and T6-treated 1 vol% SiC_{np}/7075Al with two-theta ranging from 20 to 60 degrees are shown in Fig. 9a. Their XRD full patterns are shown in Fig. S3, where the diffraction intensity of (220) crystal planes disappears, indicating the preferred grain orientation in all the extruded samples [29]. The presence of Al_2Cu peaks was identified in all materials, implying they were precipitated in advance and hard to dissolve under the low-temperature solid-solution process [30, 31]. Kenevisi et al. [32] also reported the intergranular phase of Al_2Cu was stable at the grain boundary of 7075Al alloy. A series of $MgZn_2$ (η'/η phase) peaks near 40 degrees can be clearly observed in T6-treated 7075Al and SiC_{np}/7075Al [26, 31]. The TEM observations have revealed high-density dislocations in the SiC_{np}/7075Al composite (Fig. 7e). Based on the XRD patterns in Fig. 9a, the microstrain (ε) and the microcrystallite size (d) of all the samples were estimated by the Williamson–Hall method
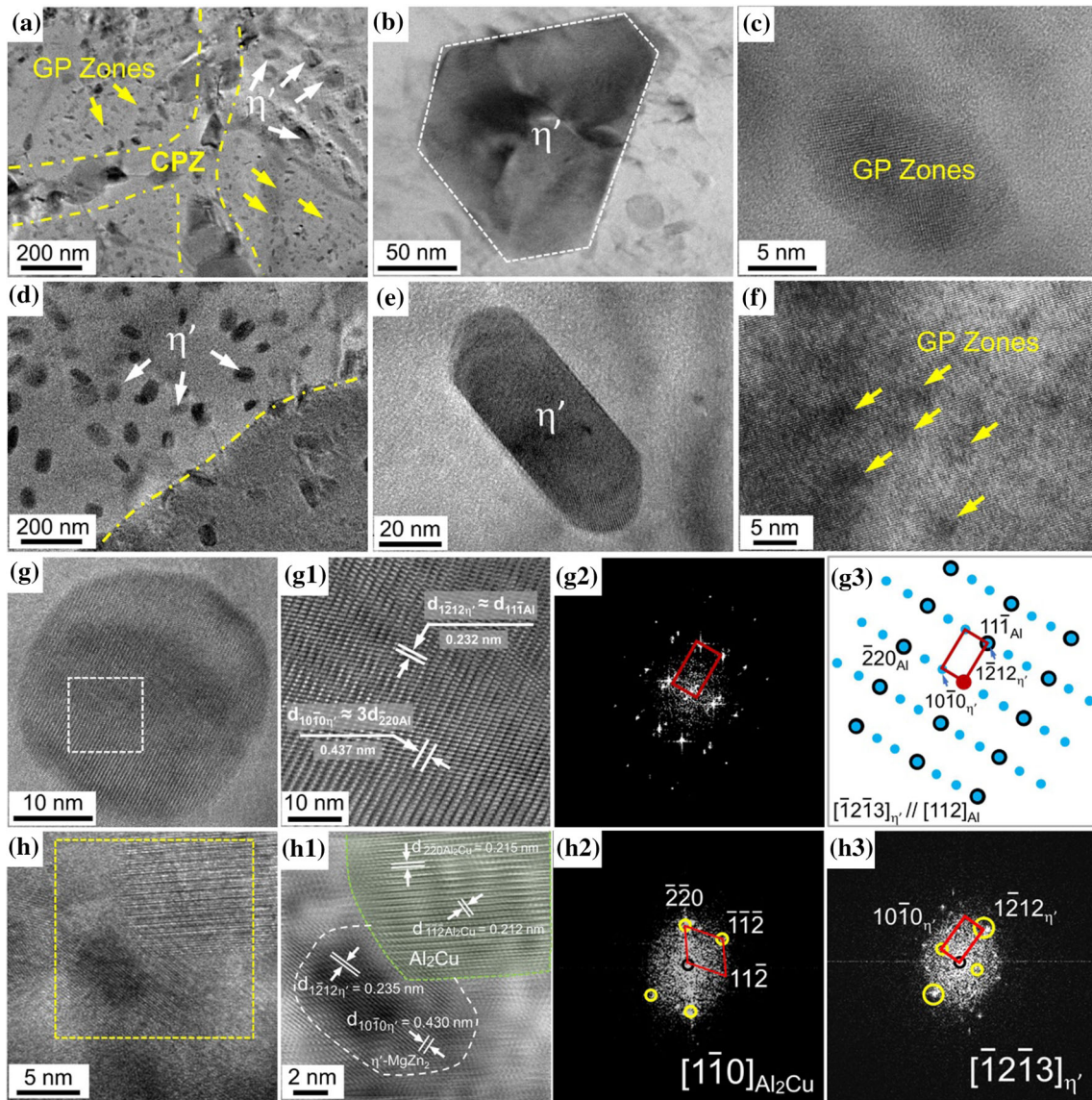
Figure 8 Representative TEM and HRTEM images for precipitation characteristics of **a**–**c** 7075Al alloy and **d**–**f** 1 vol% SiC$_{np}$/7075Al composite; **g** HRTEM image of η′ phase, the corresponding crystallographic analysis of **g1** inverse FFT image and **g2** FFT image, **g3** simulated diffraction patterns η′ phase; **h** HRTEM image of η′ phase and Al$_2$Cu phase, the corresponding crystallographic analysis of **h1** inverse FFT image and **h2**, **h3** FFT images.

(Fig. S4; Table S2) [33]. The dislocation densities (ρ) of them were calculated by the equation [9, 33]:

$$\rho = \frac{2\sqrt{3}\varepsilon}{db} \qquad (2)$$

where b is the Burgers vector of the matrix (0.286 nm for Al). The calculation results of dislocation densities are depicted in Table S2 and Fig. 9b. Although the dislocation density generally decreases with increasing the aging time [6], the T6-treated 7075Al (4.5×10^{14} m^{-2}) in this work has much larger dislocation density than as-quenched 7075Al

(3.9×10^{14} m^{-2}), which may result from the CPZ introducing much space mismatch in 7075Al. As a comparison, the dislocation densities of as-quenched SiC$_{np}$/7075Al and T6-treated SiC$_{np}$/7075Al are improved to be 5.3×10^{14} m^{-2} and 5.4×10^{14} m^{-2}, respectively. Attributed to the elimination of CPZ (Fig. 8d), the precipitation behavior and the annihilation of dislocations operated simultaneously and gave rise to a steady dislocation state in T6-treated SiC$_{np}$/7075Al during aging.

Figure 9 a XRD peaks (amplified range from 20 to 60 degree) and **b** calculated dislocation densities of as-quenched 7075Al, as-quenched 1 vol% SiC_{np}/7075Al, T6-treated 7075Al and T6-treated 1 vol% SiC_{np}/7075Al.
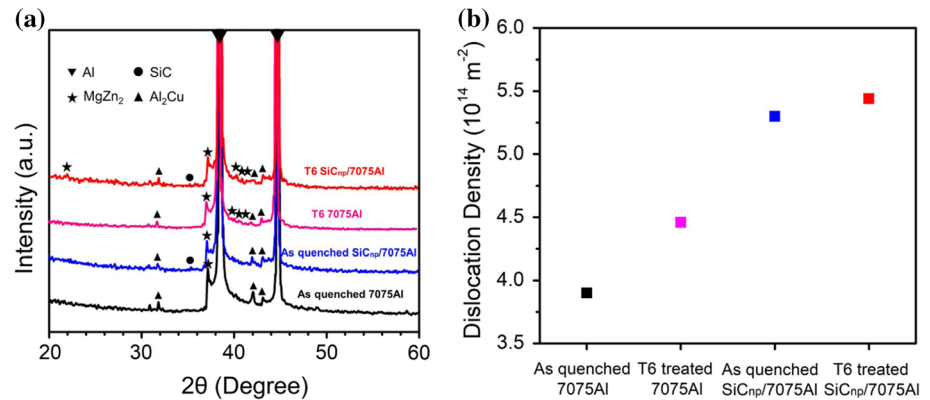
Fractography of 7075Al and SiC_{np}/7075Al composites

Figure 10 shows the SEM images of the fractured surfaces of 7075Al and SiC_{np}/7075Al composites with 0.5–1.5 vol% reinforcements from low to high magnification. All of the materials revealed typical ductile fractography consisted of homogenous fine dimples and local large dimples, while the dimple size of SiC_{np}/7075Al composites seemed more uniform and smaller, which was consistent with their higher tensile strengths. Figure 10e1–e4 shows the dimple size distributions with different SiC_{np} contents (0, 0.5, 1.0, and 1.5 vol%), and the mean dimple diameters were counted to be ~ 2.31 μm, ~ 1.01 μm, ~ 0.60 μm, and ~ 1.75 μm, respectively.

Besides, the broken and pulled-out nanoparticles are observed under the high-magnified fracture morphology of 1 vol% SiC_{np}/7075Al composites (Fig. 11a). A region with the centralized distribution of some small dimples and nanoparticles (marked by yellow line box) was selected to conduct a semi-quantitative analysis of EDS scan (Fig. 11b). The results are consistent with the contained elements in the composites and show the nanoparticles are almost corresponding to the precipitated phases. To further confirm the composition of the nanoparticles, point-EDS was performed for one of them (marked with yellow circle district in Fig. 11c), the result of which is shown in Fig. 11d. Mg, Zn, and Cu as the main elements of precipitated phases were identified, and the atom ratio of Mg to Zn was roughly detected as 1:1 rather than an accurate composition of $MgZn_2$ (η′ phase). This can be attributed to the influence of some amounts of uniformly dispersed GP zones in the matrix caught by the penetrating electron beam of SEM.

Discussion

Optimization mechanism of precipitation behavior in SiC_{np}/7075Al composites

The precipitation behavior in SiC_{np}/7075Al composites has demonstrated the following features by atomic-scale investigation: (1) No obvious CPZs or PFZs were found and the uniform-sized precipitates were well distributed (Fig. 8d); (2) η′ phase precipitates were proved to have a compatible crystallographic relationship with Al matrix (Fig. 8g1–g3); (3) A semi-coherent interface between η′ phase and pre-precipitated Al_2Cu phase was revealed with a relatively low interfacial mismatch (Fig. 8h1), which is beneficial to the formation and growth of η′ phase taking Al_2Cu phase as a nucleation site. As a normal precipitation sequence of 7075Al alloy, GP zones, metastable η′ phases, and equilibrium η phase were still identified in peak-aged SiC_{np}/7075Al composite. However, compared with the 7075Al alloy matrix, the experimental results indicate that the addition of SiC_{np} changed the kinetics of precipitation and morphology of precipitates without changing their sequence.

Commonly, a homogenous distribution of GP zones and η′ phases can precipitate from solid state during aging treatment in 7075Al alloy [4, 8]. The formation of CPZ and PFZ herein was supposed to be introduced by the thermo-elastic stress-induced dislocations (TSDs) and grain boundary vacancy depletion, which were originated from the hot-extrusion process before [6, 31]. Solute atoms diffused fast toward dislocations with the help of TSDs resulting in the formation of coarse precipitates. The thermal plastic deformation of hot extrusion caused the dynamic recrystallization of Al grains, and those
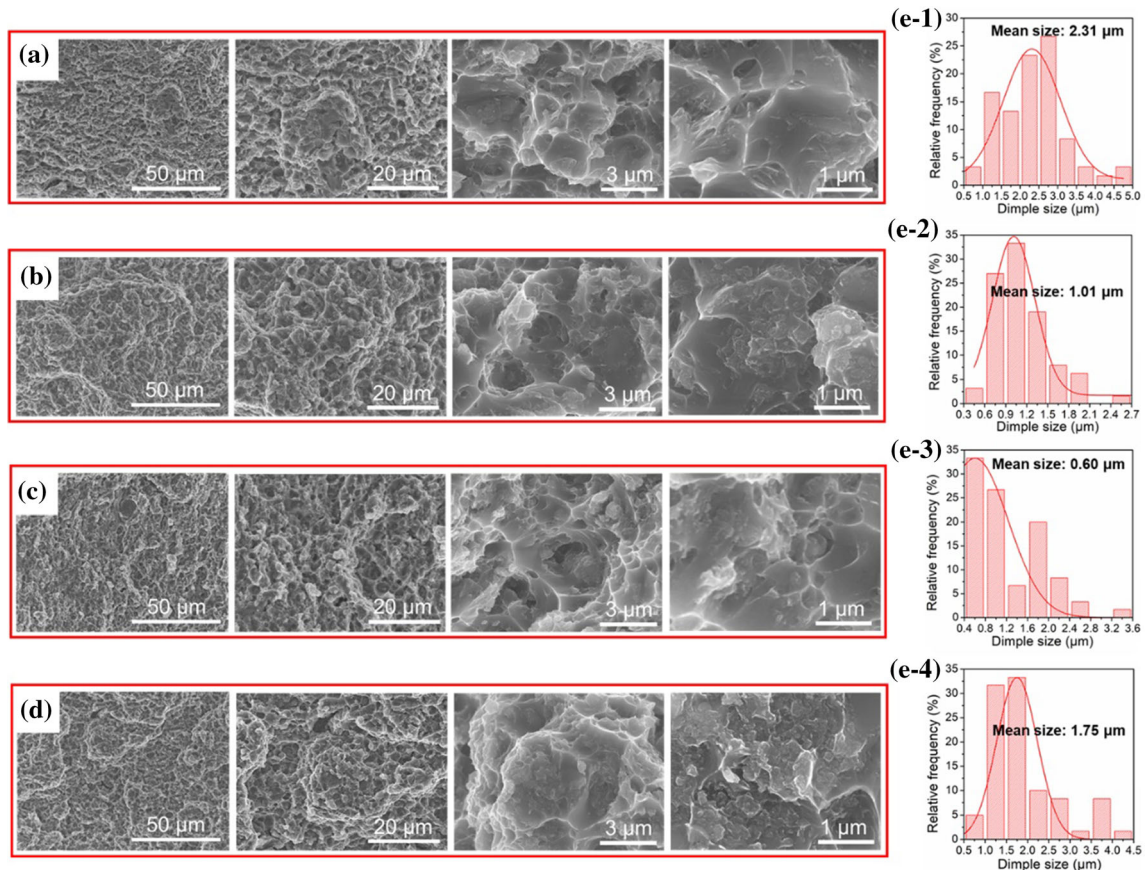
Figure 10 **a–d** SEM tensile fracture surfaces of 7075Al and SiC$_{np}$/7075Al bulk composites with SiC$_{np}$ content of 0.5, 1.0, and 1.5 vol%. **e** The statistics charts of the dimple diameter distributions.

recrystallized high-angle grain boundaries were ideal sinks to absorb and annihilate vacancies during the solution treatment [6, 8]. Therefore, the small GP zones with a higher amount and coarsened η′ phases with a lower amount are representative precipitation in 7075Al alloy in this work. For the SiC$_{np}$/7075Al composite, the movement of SiC$_{np}$ and the plastic flow of Al grains during extrusion would interact with each other; thus, the recrystallization and growth of Al grains were constrained. The PFZ formation was removed by the depression of the vacancy concentration difference. The interfacial mismatch between SiC$_{np}$ and Al matrix when hot extrusion and heat treatments initiated lots of dislocations entangling around their interfaces. These dislocations were subsequently inter-locked by solute atoms during solid-solution process. The nucleation and continuous growth of precipitates during aging were accelerated by short-circuiting diffusion paths composed of such solute-containing dislocations [34, 35]. By this optimization mechanism, fine GP

zones and uniform-sized η′ phase were obtained in SiC$_{np}$/7075Al composite with overall improved mechanical properties, avoiding the impact of CPZs [6, 23, 24]. Moreover, the elements of Al and Cu were detected by EDS mapping having a good match of atomic positions with Zn and Mg in precipitates (Fig. 7f), but Cu and Al did not affect the crystal structure of the precipitate phases in SiC$_{np}$/7075Al (Fig. 9a). As a kind of pre-precipitated phase, the Al$_2$Cu phase has a semi-coherent interface with η′ phase (Fig. 8h), which is of relatively low interfacial energy and beneficial to the preferential formation of η′ phases nearby Al$_2$Cu phases. The SiC$_{np}$ were proved to promote the pre-precipitation of Al$_2$Cu phases (Fig. 4c, d); thus, they could also affect the precipitation of η′ phases indirectly.

Figure 11 **a**, **c** High-magnification SEM fractography of 1 vol% SiC$_{np}$/7075Al, **b**, **d** the corresponding selected area and point energy spectrums.
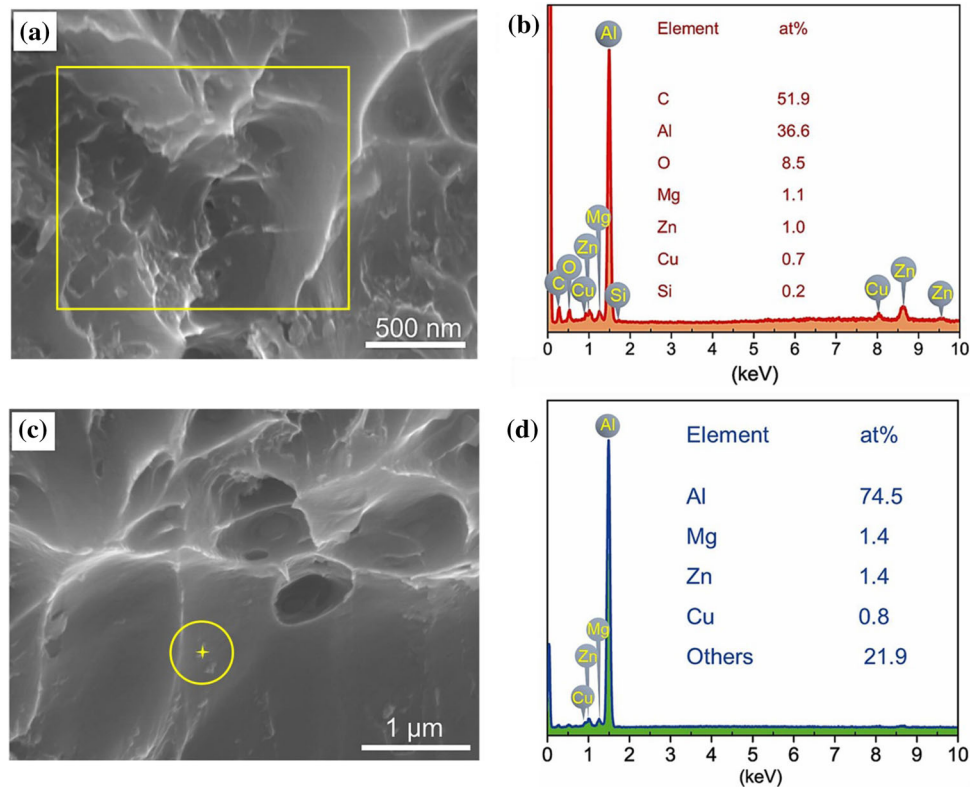
Strengthening mechanism in peak-aged SiC$_{np}$/7075Al composite

With the characterization of the microstructures and various precipitation behaviors between 7075Al alloy and SiC$_{np}$/7075Al composite, there are three possible strengthening mechanisms in peak-aged SiC$_{np}$/7075Al: (1) grain refinement ($\Delta\sigma_{GR}$), due to the grain boundaries pinning and plastic deformation; (2) geometrically necessary dislocation strengthening ($\Delta\sigma_{GND}$) due to an increase in dislocation density caused by thermal expansion mismatch and elastic modulus mismatch; and (3) precipitate and dispersoid strengthening ($\Delta\sigma_{P–D}$) governed by either the dislocation shearing or Orowan dislocation bypassing mechanisms. Among them, the effect of grain refinement could be calculated by classical Hall–Petch equation [36]:

$$\Delta\sigma_{GR} = K\left(d_c^{-\frac{1}{2}} - d_m^{-\frac{1}{2}}\right) \tag{3}$$

where K is a constant (0.04 MPa m$^{1/2}$ for Al [9, 33]) and d_c and d_m are the average gain size of composite and matrix, respectively. The $\Delta\sigma_{GR}$ mainly depends on the grain size. From the XRD results (Table S2) and TEM observation (Fig. 7 and 8), the d_c is similar

to d_m; thus, the grain refinement was neglected. Therefore, the $\Delta\sigma_{GND}$ and $\Delta\sigma_{P–D}$ are the major strengthening mechanisms working in the present composite.

The increase in dislocation density in SiC$_{np}$/7075Al composites, especially at the as-quenched state, originates from the different thermal mismatches between the SiC$_{np}$ and matrix, which plays an indispensable role in blocking the motivation of dislocations. Additionally, the difference of elastic modulus and yield strength between SiC$_{np}$ and matrix usually leads to the accumulation of dislocation during a mechanical response. Hence, the density of geometrically necessary dislocations (ρ_{GND}) was calculated (calculation details in see Supporting Information) and the contributed strength stemming from the increasing ρ_{GND} can be expressed as follows [23, 37]:

$$\Delta\sigma_{GND} = M\alpha Gb\sqrt{\rho_{GND}} \tag{4}$$

where M (3.06 for fcc metal) is mean orientation factor, α (0.2) is a constant, G (26 GPa for Al [35]) is shear modulus, and ρ_{GND} is equal to 8.39×10^{13} m^{-2}. Assuming the SiC$_{np}$ are uniformly distributed in the matrix, the theoretically estimated upper limit of the $\Delta\sigma_{GND}$ in peak-aged 1 vol% SiC$_{np}$/7075Al composite

is 41.7 MPa. Compared with the 7075Al alloy, the actual increase in the yield strength of the 1 vol% SiC_{np}/7075Al composite was $\sim$ 72 MPa. The residual contribution of the strength ($\sim$ 30.3 MPa) could be originated from the $\Delta\sigma_{P-D}$ by optimized precipitation behavior.

The precipitates and dispersoids including GP zones, $MgZn_2$ (η'/η) phases, and Al_2Cu phases were observed in peak-aged 7075Al matrix and SiC_{np}/7075Al composite. In general, the operative mechanism of the incoherent η phase and Al_2Cu phase is Orowan dislocation bypassing ($\Delta\sigma_{OR}$) and it can be estimated according to the formula of Orowan–Ashby [23, 38]:

$$\Delta\sigma_{OR} = \frac{0.4MGb}{\pi(1-v)^{1/2}\lambda_p}\ln\left(\frac{2\bar{r}}{b}\right) \quad (5)$$

where v is the Poisson's ratio of the matrix (0.33 for Al) and λ_p is the effective planar inter-particle spacing. $\bar{r}$ is the mean radius of a random circular cross-plane for a spherical precipitate and could be obtained by: $\bar{r} = \sqrt{2/3}r$, where r is the average radius of the dispersed hard precipitate particles. The operative mechanism of coherent or semi-coherent GP zones and η' phase precipitates is difficult to quantitatively estimate because dislocation shearing is determined by the intrinsic properties of materials. To simplify this discussion, $\Delta\sigma_{OR}$ is regarded as the upper bound value of $\Delta\sigma_{P-D}$ for all the precipitates and dispersoids in the matrix [24]. Since the SiC_{np} are almost dispersed at the grain boundary of composite, the resistance of the closely spaced SiC_{np} to the motion of dislocations was attributed to the $\Delta\sigma_{GND}$ we discussed above. For $\Delta\sigma_{OR}$, the parameters of matrix and composite in Eq. (5) were marked by $\bar{r}_1$, r_1, λ_{p1}, and $\bar{r}_2$, r_2, λ_{p2}, respectively. To prove the relative superiority of the precipitates in composite over in matrix, the ratio of their $\Delta\sigma_{OR}$ was conducted, which is denoted as Δ_{Ratio} and expressed as the following equation:

$$\Delta Ratio = \frac{\Delta\sigma_{OR(matrix)}}{\Delta\sigma_{OR(composite)}} = \frac{\ln\left(\frac{2\bar{r}_1}{b}\right)\cdot\lambda_{p2}}{\ln\left(\frac{2\bar{r}_2}{b}\right)\cdot\lambda_{p1}} \quad (6)$$

where λ_{p1} and λ_{p2} could be calculated as follows [37]:

$$\lambda_p = 2\sqrt{\frac{2}{3}}r\left(\sqrt{\frac{\pi}{4V_p}} - 1\right) \quad (7)$$

where V_p is the volume fraction of the precipitates inside both grains of the matrix and composites and

the values of them are approximately identical ($V_{p1} \approx V_{p2}$). Consequently, based on Eq. (7), the expression of Δ_{Ratio} could be simplified to the following form:

$$\Delta Ratio = \frac{\Delta\sigma_{OR(matrix)}}{\Delta\sigma_{OR(composite)}} = \frac{\ln\left(\frac{2\sqrt{2/3}r_1}{b}\right)r_2}{\ln\left(\frac{2\sqrt{2/3}r_2}{b}\right)r_1} \quad (8)$$

It is found that the value of Δ_{Ratio} is only affected by the precipitate particle size, namely the value of r. When substituting the values of r_1 and r_2 with the statistical results of 83.4 and 48.7 nm (Fig. S5), the value of Δ_{Ratio} is 0.64, which is less than 1, thus indicating the role of $\Delta\sigma_{OR}$ on the composite is more significant than that on matrix. In summary, the strength increments of mechanical property in peak-aged SiC_{np}/7075Al composites are not only influenced by the dislocation strengthening that resulted from SiC_{np} reinforcements, but also relevant to its optimized precipitation strengthening.

Fracture modes of peak-aged 7075Al and SiC_{np}/7075Al

According to the results analysis of microstructure and fractography, the different fracture modes of 7075Al and SiC_{np}/7075Al in this study influenced by precipitation behaviors have been proposed, as shown in Fig. 12.

The cracks propagation path of 7075Al alloy is illustrated in Fig. 12a. The fracture is usually easy to take place in 7075Al alloy when tensile due to the formation of stress concentration and crack initiation arose from coarse precipitates at the grain boundary and in CPZ [8, 13]. From the above discussion, the coarse precipitates either at the grain boundary or in CPZ are mainly platelet η' phase and pre-precipitated Al_2Cu phases. Many large dimples were observed in the fracture surface of 7075Al alloy with precipitates along the dimple edges (Fig. 10a). As far as concerned of the SiC_{np}/7075Al composite, the SiC_{np} distributed at grain boundaries improve grain boundary energy and trigger the dislocations in the vicinity of it through the thermal mismatch. The well-distributed precipitates are found in SiC_{np}/7075Al, because of the elimination of PFZ and CPZ, as well as the heterogeneous nucleation of platelet η' phase and Al_2Cu phases led by high-dense dislocations [24, 34].

Figure 12 The schematic illustration of the fracture modes and crack propagation behaviors of 7075Al and SiC$_{np}$/7075Al composite.
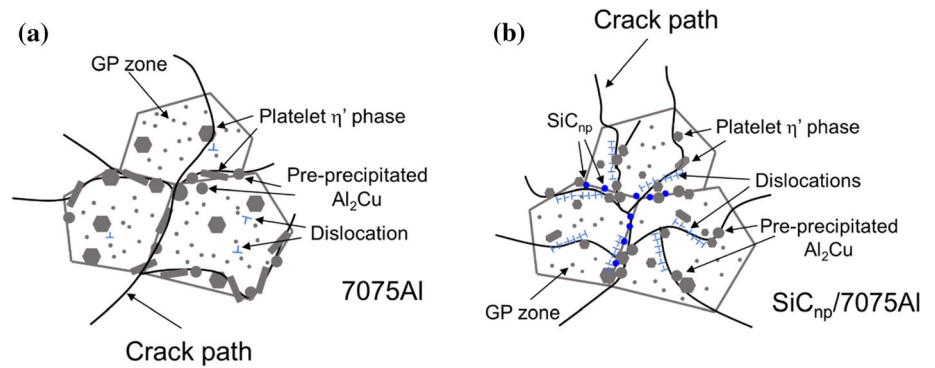
The debonding of precipitate with the matrix is dominant for crack initiation; thus, the size of the dimples depends on the distribution of the precipitates. The remission of stress concentration and the deflection of the crack propagation path give rise to that the large dimples are not evident in SiC$_{np}$/7075Al composites (Fig. 10b–d). The typical fracture mode illustration of SiCnp/7075Al caused by its optimization of precipitation behavior is exhibited in Fig. 12b.

Conclusions

7075Al alloy matrix composites with 0, 0.5, 1.0, and 1.5 vol% SiC$_{np}$ were fabricated by shift-speed ball milling method with subsequent hot-press sintering, hot extrusion, and T6 heat treatment. The effect of SiC$_{np}$ on the mechanical properties and precipitation behavior of 7075 alloys was studied. The main conclusions are summarized as follows:

1. The tensile strength of 7075Al alloy was enhanced by a small addition of SiC$_{np}$. The SiC$_{np}$/7075Al composite had the highest strength value with SiC$_{np}$ content of 1.0 vol%, exhibiting a YS of 559 MPa and UTS of 609 MPa. The main operative mechanisms by SiC$_{np}$ were attributed to geometrically necessary dislocation strengthening and optimized precipitation strengthening.

2. The addition of SiC$_{np}$ caused a lot of induced dislocations due to interfacial mismatch with the Al matrix during hot extrusion and heat treatment. These dislocations, entangled around the grain boundaries and pinned solute atoms, were contributed to the formation of fine GP zones and uniform-sized η' phase in SiC$_{np}$/7075 composite. SiC$_{np}$ also indirectly affected the precipitation of

η' phase by promoting pre-precipitates. Hence, this study suggests a strategy for the design of alloy matrix composites by using nano-reinforcements to optimize the precipitation.

Author's contribution

BP contributed to experiment, characterization, and writing of the original draft. XL was involved in the investigation, experiment, and characterization. BL contributed to experiment and characterization. XC was involved in the analysis, and revising. CH was involved in the validation, resources, and supervision. NZ contributed to revising, validation, and project administration.

Compliance with ethical standards

Conflict of interest The authors declare that they have no known competing financial interests or personal relationships that could have appeared to influence the work reported in this paper.

Electronic supplementary material: The online version of this article (https://doi.org/10.1007/s10853-020-04381-4) contains supplementary material, which is available to authorized users.

References

[1] Williams JC, Starke EA (2003) Progress in structural materials for aerospace systems. Acta Mater 51:5775–5799

[2] Bayazid SM, Farhangi H, Asgharzadeh H (2016) Effect of cyclic solution treatment on microstructure and mechanical properties of friction stir welded 7075 Al alloy. Mater Sci Eng A 649:293–300

[3] Das P, Jayaganthan R, Singh IV (2011) Tensile and impact-toughness behaviour of cryorolled Al 7075 alloy. Mater Des 32:1298–1305

[4] Li Z, Xiong B, Zhang Y et al (2008) Investigation of microstructural evolution and mechanical properties during two-step ageing treatment at 115 and 160 °C in an Al–Zn–Mg–Cu alloy pre-stretched thick plate. Mater Charact 59:278–282

[5] Fang X, Song M, Li K et al (2012) Effects of Cu and Al on the crystal structure and composition of η (MgZn$_2$) phase in over-aged Al–Zn–Mg–Cu alloys. J Mater Sci 47:5419–5427. https://doi.org/10.1007/s10853-012-6428-9

[6] Li H, Chen P, Wang Z et al (2019) Tensile properties, microstructures and fracture behaviors of an Al–Zn–Mg–Cu alloy during ageing after solution treating and cold-rolling. Mater Sci Eng A 742:798–812

[7] Liu JZ, Chen JH, Yuan DW et al (2015) Fine precipitation scenarios of AlZnMg (Cu) alloys revealed by advanced atomic-resolution electron microscopy study part I: structure determination of the precipitates in AlZnMg (Cu) alloys. Mater Charact 99:277–286

[8] Yang W, Ji S, Zhang Q et al (2015) Investigation of mechanical and corrosion properties of an Al–Zn–Mg–Cu alloy under various ageing conditions and interface analysis of η′ precipitate. Mater Des 85:752–761

[9] Zhao YH, Liao XZ, Jin Z et al (2004) Microstructures and mechanical properties of ultrafine grained 7075 Al alloy processed by ECAP and their evolutions during annealing. Acta Mater 52:4589–4599

[10] Wang ZG, Li CP, Wang HY et al (2016) Effect of nano-SiC content on mechanical properties of SiC/2014Al composites fabricated by powder metallurgy combined with hot extrusion. Powder Metall 59:236–241

[11] Wu RR, Yuan Z, Li QS (2017) Microstructure and mechanical properties of 7075 Al alloy based composites with Al$_2$O$_3$ nanoparticles. Int J Cast Metal Res 30:337–340

[12] Jiang J, Wang Y (2015) Microstructure and mechanical properties of the semisolid slurries and rheoformed component of nano-sized SiC/7075 aluminum matrix composite prepared by ultrasonic-assisted semisolid stirring. Mater Sci Eng A 639:350–358

[13] Ye T, Xu Y, Ren J (2019) Effects of SiC particle size on mechanical properties of SiC particle reinforced aluminum metal matrix composite. Mater Sci Eng A 753:146–155

[14] Guo X, Guo Q, Nie J et al (2018) Particle size effect on the interfacial properties of SiC particle-reinforced Al–Cu–Mg composites. Mater Sci Eng A 711:643–649

[15] Jiang L, Wen H, Yang H et al (2015) Influence of length-scales on spatial distribution and interfacial characteristics of B$_4$C in a nanostructured Al matrix. Acta Mater 89:327–343

[16] Wang Z, Li C, Wang H et al (2016) Aging behavior of nano-SiC/2014Al composite fabricated by powder metallurgy and hot extrusion techniques. J Mater Sci Technol 32:1008–1012

[17] Xu R, Tan Z, Fan G et al (2018) High-strength CNT/Al–Zn–Mg–Cu composites with improved ductility achieved by flake powder metallurgy via elemental alloying. Compos A 111:1–11

[18] Jiang Y, Tan Z, Xu R et al (2018) Tailoring the structure and mechanical properties of graphene nanosheet/aluminum composites by flake powder metallurgy via shift-speed ball milling. Compos A 111:73–82

[19] Liu Y, Yang C, Chen W et al (2014) Effects of particle size and properties on the microstructures, mechanical properties, and fracture mechanisms of 7075Al hybrid composites prepared by squeeze casting. J Mater Sci 49:7855–7863. https://doi.org/10.1007/s10853-014-8496-5

[20] Luo ZP, Song YG, Zhang SQ (2001) A TEM study of the microstructure of SiCp/Al composite prepared by pressure-less infiltration method. Scr Mater 45:1183–1189

[21] Chen X, Zhou W, Feng Q et al (2016) Irradiation effects in 6H–SiC induced by neutron and heavy ions: Raman spectroscopy and high-resolution XRD analysis. J Nucl Mater 478:215–221

[22] Guo B, Chen B, Zhang X et al (2018) Exploring the size effects of Al$_4$C$_3$ on the mechanical properties and thermal behaviors of Al-based composites reinforced by SiC and carbon nanotubes. Carbon 135:224–235

[23] Mazzer EM, Afonso CRM, Galano M et al (2013) Microstructure evolution and mechanical properties of Al–Zn–Mg–Cu alloy reprocessed by spray-forming and heat treated at peak aged condition. J Alloys Compd 579:169–173

[24] Ma K, Wen H, Hu T et al (2014) Mechanical behavior and strengthening mechanisms in ultrafine grain precipitation-strengthened aluminum alloy. Acta Mater 62:141–155

[25] Ma GN, Wang D, Liu ZY et al (2019) An investigation on particle weakening in T6-treated SiC/Al–Zn–Mg–Cu composites. Mater Charact 158:109966

[26] Lu T, Chen W, Xu W et al (2018) The effects of Cr particles addition on the aging behavior and mechanical properties of SiCp/7075Al composites. Mater Charact 136:264–271

[27] Xu X, Zheng J, Li Z et al (2017) Precipitation in an Al–Zn–Mg–Cu alloy during isothermal aging: atomic-scale HAADF-STEM investigation. Mater Sci Eng A 691:60–70

[28] Pilania G, Thijsse BJ, Hoagland RG et al (2014) Revisiting the Al/Al$_2$O$_3$ interface: coherent interfaces and misfit accommodation. Sci Rep 4:4485

[29] Mokdad F, Chen DL, Liu ZY et al (2016) Deformation and strengthening mechanisms of a carbon nanotube reinforced aluminum composite. Carbon 104:64–77

[30] Shaeri MH, Salehi MT, Seyyedein SH et al (2014) Microstructure and mechanical properties of Al-7075 alloy processed by equal channel angular pressing combined with aging treatment. Mater Des 57:250–257

[31] Yin X, Deng W, Zou Y et al (2019) Ultrafine grained Al 7075 alloy fabricated by cryogenic temperature large strain extrusion machining combined with aging treatment. Mater Sci Eng A 762:138106

[32] Kenevisi MS, Mousavi-Khoie SM (2012) An investigation on microstructure and mechanical properties of Al7075 to Ti–6Al–4V transient liquid phase (TLP) bonded joint. Mater Des 38:19–25

[33] Williamson GK, Hall WH (1953) X-ray line broadening from filed aluminium and wolfram. Acta Metall 1:22–31

[34] Wu C, Ma K, Zhang D et al (2017) Precipitation phenomena in Al–Zn–Mg alloy matrix composites reinforced with B$_4$C particles. Sci Rep 7:9589

[35] Feng Z, Luo X, Chen Y et al (2019) Surface severe plastic deformation induced solute and precipitate redistribution in an Al–Cu–Mg alloy. J Alloys Compd 773:585–596

[36] Hansen N (2004) Hall–Petch relation and boundary strengthening. Scr Mater 51:801–806

[37] Zhao R, Xu R, Fan G et al (2015) Reinforcement with in situ synthesized carbon nano-onions in aluminum composites fabricated by flake powder metallurgy. J Alloys Compd 650:217–223

[38] Jiang L, Yang H, Yee JK et al (2016) Toughening of aluminum matrix nanocomposites via spatial arrays of boron carbide spherical nanoparticles. Acta Mater 103:128–140